Direct measurement of emittance in the Muon Ionization Cooling Experiment

MICE collaboration

The Muon Ionization Cooling Experiment (MICE) collaboration seeks to demonstrate the feasibility of ionization cooling, the technique by which it is proposed to cool the muon beam at a future neutrino factory or muon collider. The emittance is measured from an ensemble of muons assembled from those that pass through the experiment. A pure muon ensemble is selected using a particle identification system that can reject efficiently both pions and electrons. The position and momentum of each muon is measured using a high-precision scintillating-fibre tracker in a 4 T solenoidal magnetic field. This paper presents the techniques used to reconstruct the phase-space distributions and reports the emittance of the muon beam as a function of muon-beam momentum.

1 Introduction

Stored muon beams have been proposed as the source of neutrinos at a neutrino factory [1, 2] and as the means to deliver multi-TeV lepton-antilepton collisions at a muon collider [3, 4]. In such facilities the muon beam is produced from the decay of pions generated by a high-power proton beam striking a target. The tertiary muon beam occupies a large volume in phase space. To optimise the muon yield for a neutrino factory, and luminosity for a muon collider, while maintaining a suitably small aperture in the muon-acceleration system requires that the muon beam be "cooled" (i.e. its phase-space volume reduced) prior to acceleration. An alternative approach to the production of low-emittance muon beams through the capture of $\mu^+\mu^-$ pairs close to threshold in electron–positron annihilation has recently been proposed [5]. To realise the luminosity required for a muon collider using this scheme requires the substantial challenges presented by the accumulation and acceleration of the intense positron beam, the high-power muon-production target, and the muon-capture systems to be addressed.

A muon is short-lived, with a lifetime of 2.2 μs in its rest frame. Therefore, beam manipulation at low energy (≤ 1 GeV) must be carried out rapidly. Four cooling techniques are in use at particle accelerators: synchrotron-radiation cooling [6]; laser cooling [7–9]; stochastic cooling [10]; and electron cooling [11]. In each case, the time taken to cool the beam is long compared to the muon lifetime. In contrast, ionization cooling is a process that occurs on a short timescale. A muon beam passes through a material (the absorber), loses energy, and is then re-accelerated, cooling the beam efficiently with modest decay losses. Ionization cooling is therefore the technique by which it is proposed to increase the number of particles within the downstream acceptance, for a neutrino factory, and phase-space density for a muon collider [12–14]. This technique has never been demonstrated experimentally and such a demonstration is essential for the development of future high-brightness muon accelerators.

The international Muon Ionization Cooling Experiment (MICE) has been designed [15] to perform a full demonstration of transverse ionization cooling. Intensity effects are negligible for most of the cooling channels conceived for the neutrino factory or muon collider [16]. This allows the MICE experiment to record muon trajectories one particle at a time. The MICE collaboration has constructed two solenoidal spectrometers, one placed upstream, the other downstream, of the cooling cell. An ensemble of muon trajectories is assembled offline, selecting an initial distribution based on quantities measured in the upstream particle identification detectors and upstream spectrometer. This paper describes the techniques used to reconstruct the phase-space

distributions in the spectrometers and presents a measurement of the emittance of a variety of momentum-selected muon ensembles.

2 Calculation of emittance

Emittance is a key parameter in assessing the overall performance of an accelerator [17]. The luminosity achieved by a collider is inversely proportional to the colliding beam's emittance, and therefore beams with small emittance are required.

A beam travelling through a portion of an accelerator may be described as an ensemble of particles. Consider a beam that propagates in the positive z direction of a right-handed Cartesian coordinate system, (x, y, z). The position of the i^{th} particle in the ensemble, $\mathbf{r}_i = (x_i, y_i)$, and its transverse momentum, $\mathbf{p_t}_i = (p_{xi}, p_{yi})$, then define the coordinates of the particle in transverse phase space. The normalised transverse emittance, ε_N, of the ensemble approximates the volume occupied by the particles in four-dimensional phase space and is given by:

$$\varepsilon_N = \frac{1}{m_\mu} \sqrt[4]{\det \mathcal{C}}\,; \tag{1}$$

where m_μ is the rest mass of the muon, $\mathcal{C}$ is the four-dimensional covariance matrix defined by:

$$\mathcal{C} = \begin{pmatrix} \sigma_{xx} & \sigma_{xp_x} & \sigma_{xy} & \sigma_{xp_y} \\ \sigma_{xp_x} & \sigma_{p_xp_x} & \sigma_{yp_x} & \sigma_{p_xp_y} \\ \sigma_{xy} & \sigma_{yp_x} & \sigma_{yy} & \sigma_{yp_y} \\ \sigma_{xp_y} & \sigma_{p_xp_y} & \sigma_{yp_y} & \sigma_{p_yp_y} \end{pmatrix}\,; \tag{2}$$

and

$$\sigma_{\alpha\beta} = \frac{1}{N-1}\left(\Sigma_i^N \alpha_i\beta_i - \frac{\left(\Sigma_i^N \alpha_i\right)\left(\Sigma_i^N \beta_i\right)}{N}\right)\,. \tag{3}$$

The MICE experiment is operated such that muons pass through the experiment one at a time. The phase-space coordinates of each muon are measured. An ensemble of muons that is representative of the muon beam is assembled using the measured coordinates. The normalised transverse emittance of the ensemble is then calculated by evaluating the sums necessary to construct the covariance matrix, $\mathcal{C}$, and using equation 1.

3 The Muon Ionization Cooling Experiment

The muons for MICE come from the decay of pions produced by an internal target dipping directly into the circulating proton beam in the ISIS synchrotron at the Rutherford Appleton Laboratory (RAL) [25, 26]. The burst of particles resulting from one target dip is referred to as a 'spill'. A transfer line of nine quadrupoles, two dipoles and a superconducting 'decay solenoid' selects a momentum bite and transports the beam into the experiment [22]. The small fraction of pions that remain in the beam are rejected during analysis using the time-of-flight hodoscopes and Cherenkov counters that are installed in the MICE Muon Beam line upstream of the cooling experiment [27]. A 'diffuser' is installed at the upstream end of the experiment to vary the initial emittance of the beam [22]. The diffuser introduces a variable amount of high-Z material into the beam path, varying the input beam emittance that is transported to the absorber.

A schematic diagram of the experiment is shown in figure 1. It contains an absorber/focus-coil module sandwiched between two spectrometer-solenoid modules that provide a uniform magnetic field for momentum measurement. The focus-coil module has two separate windings that can be operated with the same, or opposed, polarity. A lithium-hydride or liquid-hydrogen absorber can be placed at the centre of the focus-coil module.

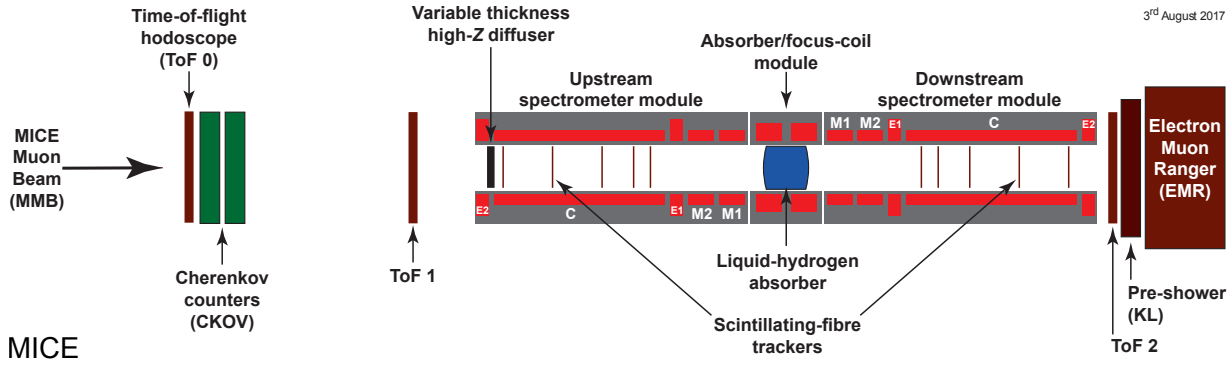

Figure 1: Schematic diagram of the configuration of the experiment. The red rectangles represent the coils of the spectrometer solenoids and focus coil. The individual coils of the spectrometer solenoids are labelled E1, C, E2, M1 and M2. The various detectors (time-of-flight hodoscopes [18, 19], Cerenkov counters [20], scintillating-fibre trackers [21], KLOE Light (KL) calorimeter [22, 23], and Electron Muon Ranger (EMR) [24]) are also represented.

The emittance is measured upstream and downstream of the absorber and focus-coil using scintillating-fibre tracking detectors [21] immersed in the solenoidal field provided by three superconducting coils (E1, C, E2). The trackers are used to reconstruct the trajectories of individual muons at the entrance and exit of the absorber. The trackers are each constructed from 5 planar stations of scintillating fibres. The track parameters are reported at the nominal reference plane; the surface of the scintillating-fibre plane closest to the absorber/focus-coil module [28]. The reconstructed tracks are combined with information from instrumentation upstream and downstream of the spectrometer modules to measure the muon-beam emittance at the upstream and downstream tracker reference planes. The instrumentation up- and downstream of the spectrometer modules is used to select a pure sample of muons. The spectrometer-solenoid modules also contain two superconducting 'matching' coils (M1, M2) that are used to match the optics between the uniform-field region and the neighbouring focus-coil.

4 MICE Muon Beam line

The MICE Muon Beam line (MMB), shown schematically in figure 2, is capable of delivering beams with normalised transverse emittance in the range $3 \leq \varepsilon_N \leq 10$ mm and mean momentum in the range $140 \leq p_\mu \leq 240$ MeV/c with a root-mean-squared (RMS) momentum spread of $\sim$20 MeV/c [22] after the diffuser (figure 1). The diffuser is situated at the entrance of the upstream spectrometer module and was used to generate a range of emittance. It consisted of tungsten and brass irises of various thickness and was operated pneumatically.

Pions produced by the momentary insertion of a titanium target [25, 26] into the ISIS proton beam are captured using a quadrupole triplet (Q1–3) and transported to a first dipole magnet (D1), which selects particles of a desired momentum bite into the 5 T decay solenoid (DS). Muons produced in pion decay in the DS are momentum-selected using a second dipole magnet (D2) and focused onto the diffuser by a quadrupole channel (Q4–6 and Q7–9). In positive-beam running, a borated polyethylene absorber of variable thickness is inserted into the beam just downstream of the decay solenoid to suppress the high rate of protons that are produced at the target [29].

The composition and momentum spectra of the beams delivered to MICE are determined by the interplay between the two bending magnets D1 and D2. In 'muon mode', D2 is set to half the current of D1, selecting backward-going muons in the pion rest frame and producing an almost pure muon beam.

Data were taken in October 2015 in muon mode at a nominal momentum of 200 MeV/c, with ISIS in opera-

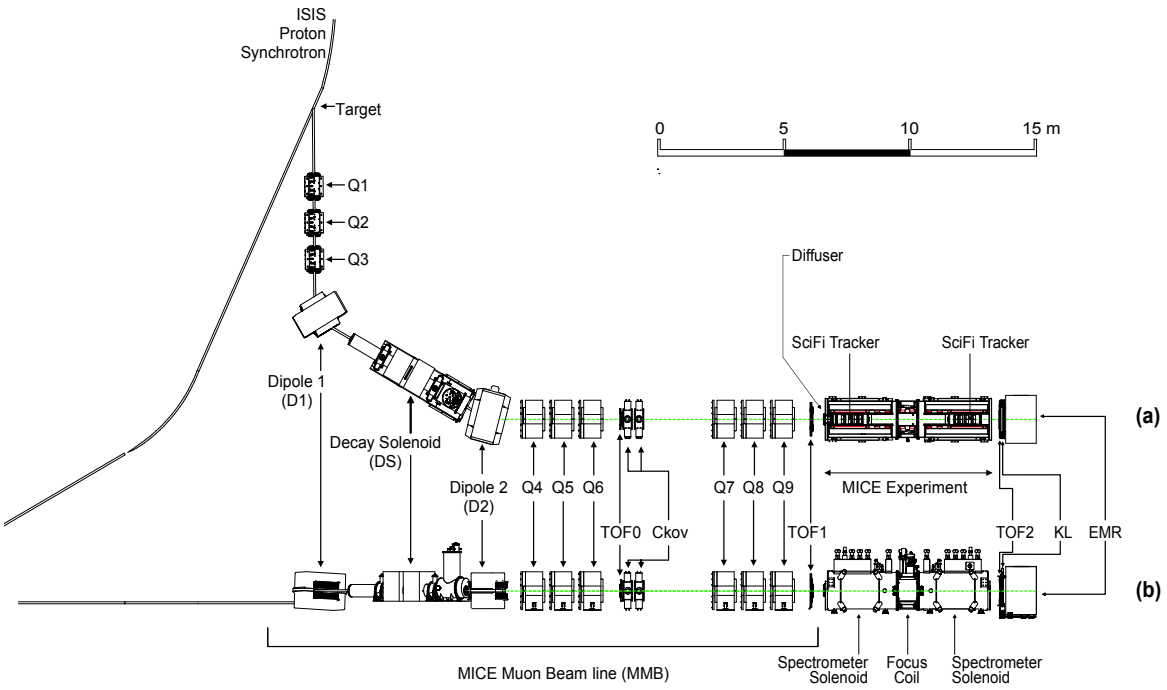

Figure 2: (a) Top and (b) side views of the MICE Muon Beam line, its instrumentation, and the experimental configuration. A titanium target dips into the ISIS proton synchrotron and the resultant spill of particles is captured with a quadrupole triplet (Q1–3) and transported through momentum-selecting dipoles (D1, D2). The final quadrupole triplets (Q4–6, Q7–9) transport particles to the upstream spectrometer module. The time-of-flight of particles, measured between TOF0 and TOF1, is used for particle identification.

tion at 700 MeV. These data are used here to characterise the properties of the beam accepted by the upstream solenoid with all diffuser irises withdrawn from the beam. The upstream E1-C-E2 coils in the spectrometer module were energised and produced a field of 4 T, effectively uniform across the tracking region, while all other coils were unpowered.

5 Simulation

Monte Carlo simulations were used to determine the accuracy of the kinematic reconstruction, to evaluate the efficiency of the response of the scintillating-fibre tracker, and to study systematic uncertainties. A sufficient number of events were generated to ensure that statistical uncertainties from the simulations were negligible in comparison to those of the data.

The beam impinging on TOF0 was produced using G4beamline [30]. Particles were produced at the target using a parameterised particle-production model. These particles were tracked through the MICE Muon Beam line taking into account all material in and surrounding the beam line and using realistic models of the field and apertures of the various magnets. The G4beamline-simulation was tuned to reproduce the observed particle distributions at TOF0.

The MICE Analysis User Software (MAUS) [31] package was used to simulate the passage of particles from TOF0 through the remainder of the MICE Muon Beam to the solenoidal lattice. This simulation includes the response of the instrumentation and used the input distribution produced using G4beamline. MAUS is used for offline reconstruction and to provide fast real-time detector reconstruction and data visualisation during MICE running. MAUS uses GEANT4 [32, 33] for beam propagation and the simulation of detector response.

The events generated were subjected to the same trigger requirements as the data and processed by the same reconstruction programs. In addition, MAUS provides a framework for data analysis. ROOT [34] is used for data visualisation and for data storage.

6 Beam selection

The experiment is read out at the end of each spill. Therefore, digital information related to the passage of the particles through the experiment is buffered in the front-end electronics and read-out at the end of the spill [22]. For the reconstructed data presented here, the digitisation of the analogue signals received from the detectors was triggered by a coincidence of signals in the two PMTs serving a single scintillator slab in TOF1. Any slab in TOF1 could generate a trigger.

The following cuts were used to select muons passing through the upstream tracker:

- *One reconstructed space-point in TOF0 and TOF1*: Each TOF hodoscope is composed of two perpendicular planes of scintillator slabs arranged to measure the x and y coordinates. A space-point is formed from the intersection of hits in the x and y projections. Figure 3 shows the hit multiplicity in TOF0 plotted against the hit multiplicity in TOF1. The sample is dominated by events with one space-point in both TOF0 and TOF1. This cut removes events in which two particles enter the experiment within the trigger window;
- *Relative time-of-flight between TOF0 and TOF1, t_{n01}, in the range $1 \leq t_{n01} \leq 6\,ns$*: The time of flight between TOF0 and TOF1 is measured relative to the mean positron time of flight, t_e. Figure 3 shows the relative time-of-flight distribution. All cuts other than the time-of-flight cut have been applied in this figure. The distance along the beam axis between TOF0 and TOF1, L, is 7.78 m. The time-of-flight of a particle between TOF0 and TOF1, t_{01}, depends on the path length travelled, $(L + s)$, where s is the additional distance travelled in the field of the quadrupole triple [27]. The time-of-flight of particles relative to the positron time-of-flight is calculated as:

$$t_{n01} = t_{01} - t_e + \frac{L + s}{c}\,;$$

  where c is the speed of light. This cut removes electrons from the selected ensemble as well as a small number of pions.
- *A single track reconstructed in the upstream tracker with a track-fit χ^2 satisfying $\frac{\chi^2}{N_{\rm DOF}} \leq 4$: $N_{\rm DOF}$* is the number of degrees of freedom. The distribution of $\frac{\chi^2}{N_{\rm DOF}}$ is shown in figure 3. This cut removes events with poorly reconstructed tracks. Multi-track events, in which more than one particle passes through the same pixel in TOF0 and TOF1 during the trigger window, are rare and are removed by this cut;
- *Track contained within the fiducial volume of the tracker*: The radius of the track at each tracker station, $R_{\rm stn}$, is required to satisfy $R_{\rm stn} < 150$ mm to ensure the track does not leave and then re-enter the fiducial volume. The track radius is evaluated at 1 mm intervals between the stations. If the track radius exceeds 150 mm at any of these positions, the event is rejected;
- *Track radius at the diffuser, $R_{\rm diff} \leq 90\,mm$*: Muons that pass through the material of the diffuser, which includes the retracted irises, lose a substantial amount of energy. Such muons may re-enter the tracking volume and be reconstructed but have properties that are no longer characteristic of the incident muon beam. The inner radius of the diffuser mechanism (100 mm) defines the transverse acceptance of the beam injected into the experiment. Back-extrapolation of tracks to the exit of the diffuser yields a measurement of $R_{\rm diff}$ with a resolution of $\sigma_{R_{\rm diff}} = 1.7$ mm. Figure 3 shows the distribution of $R_{\rm diff}$. The cut on $R_{\rm diff}$ accepts particles that passed within $5.9\sigma_{R_{\rm diff}}$ of the inner radius of the diffuser; and

Table 1: The number of particles that pass each selection criteria in isolation. A total of 24 660 particles pass all of the described cuts.

Cut	No. surviving particles	Cumulative surviving particles
None	53 276	53 276
One space-point in TOF0 and TOF1	37 619	37 619
Time of flight in range 27—32 ns	37 093	36 658
Single reconstructed track with $\frac{\chi^2}{N_{\mathrm{DOF}}} \leq 4$	40 110	30 132
Track within fiducial volume of tracker	52 039	29 714
Tracked radius at diffuser $\leq$ 90 mm	42 593	25 310
Muon hypothesis	34 121	24 660
All	24 660	24 660

- *Particle consistent with muon hypothesis:* Figure 4 shows t_{01}, the time-of-flight between TOF0 and TOF1, plotted as a function of p, the momentum reconstructed by the upstream tracking detector. The time-of-flight of a muon that loses the mean momentum measured between TOF1 and the upstream tracking detector, $\Delta p \simeq 20\,\mathrm{MeV}/c$, is also shown. Muons are accepted into the sample if the measured time-of-flight (t_{01}) is consistent with that expected, based on the measured muon momentum (p_{Tk}). To be accepted the difference between the momentum inferred from t_{01}, p_{TOF}, must satisfy $|p_{\mathrm{TOF}} - p_{\mathrm{Tk}}| < 22\,\mathrm{MeVc}$. Events for which $p_{\mathrm{TOF}} - p_{\mathrm{Tk}} > 22\,\mathrm{MeV/c}$ are ascribed to the passage of pions, or mis-reconstructed muons, and are removed from the analysis. The population of events for which $p_{\mathrm{TOF}} - p_{\mathrm{Tk}} < -22\,\mathrm{MeV/c}$ arise from muons that are poorly reconstructed or have passed through support material upstream of the tracker and have lost significant momentum. These muons are also removed from the analysis.

A total of 24 660 events pass the cuts listed above. Table 1 shows the number of particles that survive each individual cut. Data distributions are compared to the distributions obtained using the MAUS simulation in figure 3. The distribution of the time of flight between TOF0 and TOF1 is peaked towards slightly longer times in the simulation than in the data. This is related to the imperfect simulation of the distribution of longitudinal momentum of particles in the beam (see below). The distribution of $\frac{\chi^2}{N_{\mathrm{DOF}}}$ is broader and peaked at slightly larger values in the data than in the simulation. Despite these minor disagreements, the agreement between the simulation and data is sufficiently good to give confidence that a clean sample of muons has been selected.

Table 2 shows the proportions of positrons, muons, and pions in the MAUS simulation that pass all selection criteria. The expected pion contamination in the unselected ensemble of particles is 0.4% [35]. The criteria used to select the muon sample for the analysis presented here efficiently reject electrons and pions from the Monte Carlo sample.

7 Results

7.1 Phase-space projections

The distributions of x, y, p_x, p_y, p_z, and $p = \sqrt{p_x^2 + p_y^2 + p_z^2}$ are shown in figure 5. The total momentum of the muons that make up the beam lie within the range $140 \lesssim |p| \lesssim 260\,\mathrm{MeV/c}$. The results of the MAUS simulation, which are also shown in figure 5, give a reasonable description of the data. In the case of the longitudinal

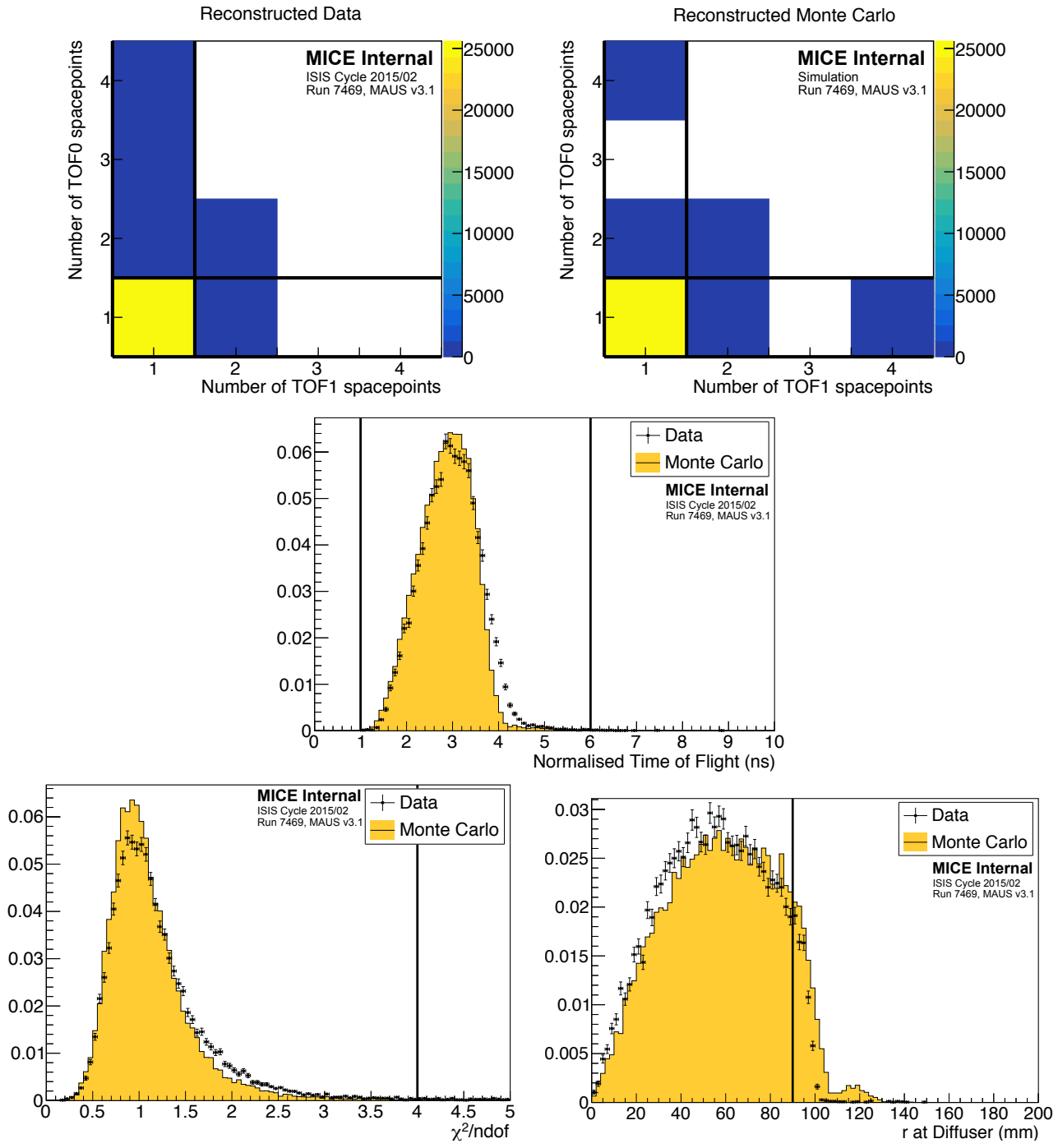

Figure 3: Distribution of the quantities that select the sample used to reconstruct the emittance of the beam. Top: the number of space-points in TOF0 plotted against the number of space-points in TOF1 (left) reconstructed data, (right) reconstructed simulation; Middle: distribution of the normalised time-of-flight, t_{n01}; Bottom left: distribution of $\frac{\chi^2}{N_{\rm DOF}}$; and Bottom right: distribution of $R_{\rm diff}$. The 1D distributions show reconstructed data as solid (black) circles and reconstructed MAUS simulation as the solid (yellow) histogram. The solid (black) lines indicate the position of the cuts made on these quantities. Events enter these plots if all cuts other than the cut under examination are passed.

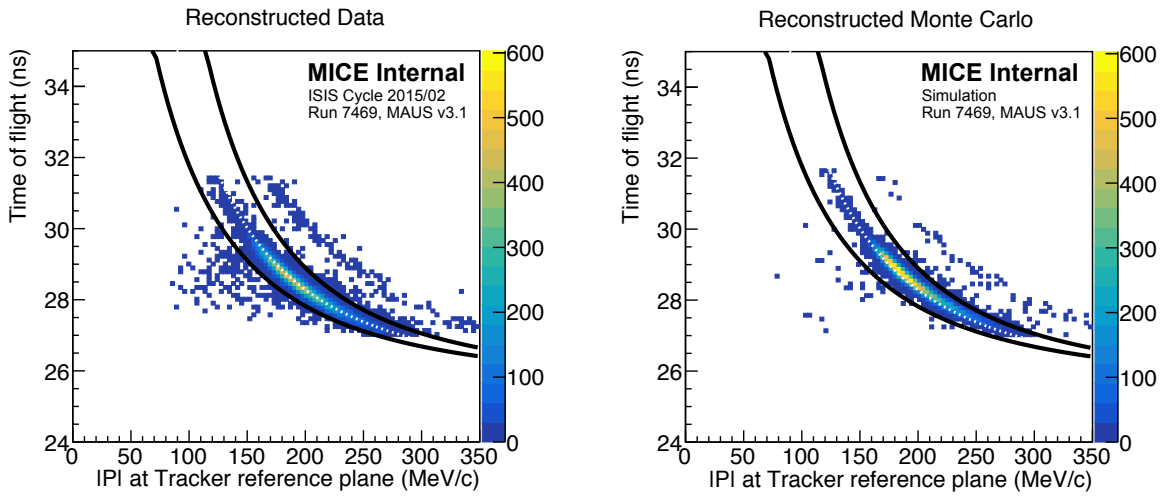

Figure 4: Time of flight between TOF0 and TOF1 (t_{01}) plotted as a function of the muon momentum, p, measured in the upstream tracker. All cuts other than the muon hypothesis have been applied. Particles within the black lines are selected as a pure muon sample. The white dotted line is the trajectory of a muon that loses the mean momentum (20 MeV/c) between TOF1 and the tracker. (Left) Reconstructed Data, (Right) Reconstructed Monte Carlo.

Table 2: The proportion of electrons, muons, and pions at the upstream tracker that survive each cut in the Monte Carlo simulation. Application of all cuts removes all but one positron and pion in the reconstructed Monte Carlo sample. A total of 25 600 particles pass all of the described cuts in the Monte Carlo simulation.

Cut	e	μ	π	Total
None	1 611	44 424	190	47 674
One space-point in TOF0 and TOF1	1224	36 317	147	38 699
Time of flight in range 27—32 ns	55	37 888	148	38 926
Single reconstructed track with $\frac{\chi^2}{N_{\mathrm{DOF}}} \leq 4$	1 197	42 486	162	43 848
Track within fiducial volume of tracker	1 581	42 458	172	44 211
Tracked radius at diffuser $\leq$ 90 mm	1 304	31 200	107	32 611
Muon hypothesis (above lower limit)	345	37 398	152	37 895
Muon hypothesis (below upper limit)	1424	42 263	39	44 106
Muon hypothesis (overall)	297	37 054	37	37 390
All	1	25 598	1	25 600

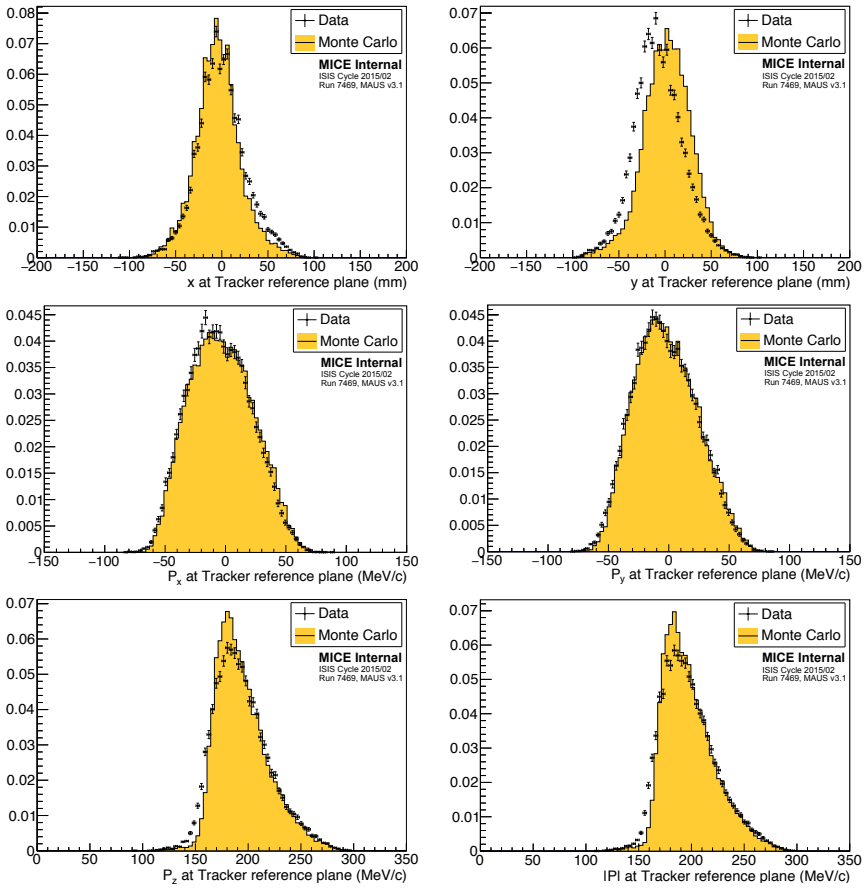

Figure 5: Position and momentum distributions of muons reconstructed at the reference surface of the upstream tracker. The top left and top right panels show the distributions of x and y respectively. The transverse components of the muon momentum are shown in the middle row; p_x in the left-middle panel, p_y in the centre middle panel. The bottom row shows the longitudinal momentum, p_z, in the bottom-left panel, and the total momentum, p, is shown in the bottom-right panel. The data is shown as the solid circles while the results of the MAUS simulation are shown as the yellow histogram.

component of momentum, p_z, the data is peaked to slightly larger values than the simulation. The difference is small and is reflected in the distribution of the total momentum, p. The distributions of the components of the transverse phase space (x, p_x, y, p_y) are well described by the simulation, with the exception of a deviation in the position of the beam in the y direction that persists across the tracking volume. This difference in the y distribution indicates that the beam centre in the vertical plane in the simulation is slightly higher than in the data.

The phase space occupied by the selected beam is shown in figure 6. The distributions are plotted at the reference surface of the upstream tracker. The beam is moderately well centred in the (x, y) plane. Correlations are apparent that couple the position and momentum components in the transverse plane. The transverse position and momentum coordinates are also seen to be correlated with total momentum. The dispersion and chromaticity of the beam is discussed further in section 7.2.

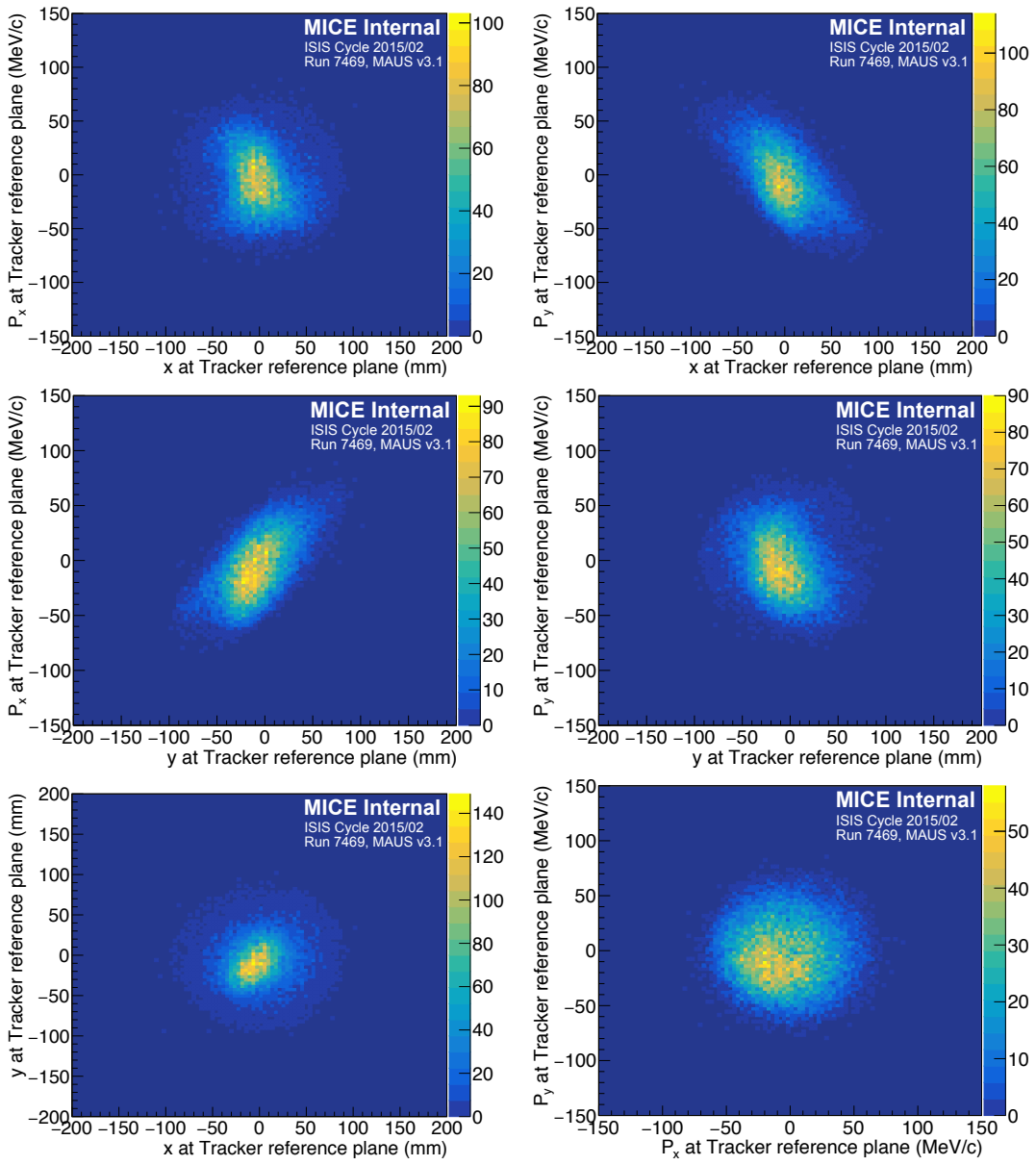

Figure 6: Transverse phase space occupied by selected muons transported through the MICE Muon Beam line to the reference plane of the upstream tracker. Top left: (x, p_x), top right: (x, p_y). Middle left: (y, p_x), middle right: (y, p_y). Bottom left: (x, y), bottom right: (p_x, p_y).

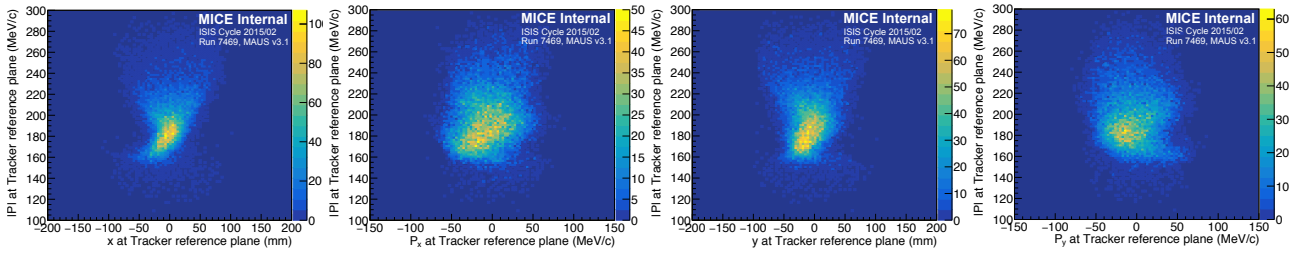

Figure 7: Dispersion is shown, from left to right, in x, p_x, y, and p_y, with respect to the longitudinal momentum, p, measured at the upstream-tracker reference plane.

7.2 Dispersion, chromaticity, and binning in longitudinal momentum

Momentum selection at D2 introduces a correlation between position and momentum. Figure 7 shows the transverse position and momentum with respect to the momentum, p, as measured at the upstream-tracker reference plane. Correlations exist between all four transverse phase-space co-ordinates and the longitudinal momentum.

Emittance is calculated in $10\,\text{MeV}/c$ bins of total momentum, p, in the range $185 \leq p \leq 255\,\text{MeV}/c$. This bin size was chosen as it is commensurate with the detector resolution. Dividing the emittance calculation into momentum increments allows for the optical mismatch of the beam to be accounted for appropriately. The range of $185 \leq p \leq 255\,\text{MeV}/c$ was chosen to maximise the number of particles in each bin that are not scraped by the aperture of the diffuser.

7.3 Uncertainties on Emittance Measurement

7.3.1 Statistical uncertainties

The statistical uncertainty on the emittance of each momentum bin is calculated as $\sigma_\varepsilon = \frac{\varepsilon}{\sqrt{2N}}$ [36–38], where ε is the emittance of the ensemble of muons in the specified momentum range and N is the number of muons in that ensemble. The number of events per bin varies from $\sim 4\,000$ for $p \sim 190\,\text{MeV}/c$ to ~ 700 for $p \sim 250\,\text{MeV}/c$.

7.4 Systematic uncertainties

Systematic uncertainties related to the beam selection were estimated by varying the cut values by an amount corresponding to the RMS resolution of the quantity in question. Systematic uncertainties related to possible biases in calibration constants were evaluated by varying each calibration constant in line with its resolution. Systematic uncertainties related to the reconstruction algorithms were evaluated using the MAUS simulation. The positive and negative deviations from the nominal emittance were added in quadrature separately to obtain the total positive and negative systematic uncertainly. Sources of uncorrelated and correlated uncertainties are discussed in detail below.

7.4.1 Uncorrelated systematic uncertainties

Systematic uncertainties related to beam selection have been estimated by varying the cut values according to the RMS resolution of the cut variables. The emittance of these ensembles was compared to the nominal selection in each momentum bin. The overall uncertainty due to beam selection is summarised in table 3. The dominant beam-selection uncertainty is in the selection of particles that successfully pass within the inner 90 mm of the diffuser aperture.

7.4.2 Correlated systematic uncertainties

Some systematic uncertainties are correlated with the total momentum, p. For example, the measured value of p dictates the momentum bin a muon is assigned to for the emittance calculation. The uncertainty on the emittance reconstructed in each bin has been evaluated by allowing the momentum of each muon to fluctuate

around its measured value according to a Gaussian distribution of width equal to the measurement uncertainty on p. In table 3 this uncertainty is listed as 'Binning in p'.

A second uncertainty that may be correlated with total momentum is the uncertainty on the reconstructed x, p_x, y, p_y. The effect on the emittance was evaluated using a procedure equivalent to that used to evaluate the uncertainty related to binning in total momentum. This uncertainty is listed as 'Tracker resolution' in table 3.

Systematic uncertainties correlated with p are primarily due to the differences between the model of the apparatus used in the reconstruction and the hardware actually used in the experiment. The most significant contribution arises from the magnetic field within the tracking volume. Particle tracks are reconstructed assuming a uniform solenoidal field, with no fringe-field effects. Small non-uniformities in the magnetic field in the tracking volume will result in a disagreement between the true parameters and the reconstructed values. To quantify this effect, six field models (one optimal and five additional models) were used to estimate the deviation in reconstructed emittance from the true value under realistic conditions. Three families of field model were investigated, corresponding to the three key field descriptors: field scale, field alignment, and field uniformity. The values of these descriptors that best described the Hall-probe measurements were used to define the optimal model and the uncertainty in the descriptor values were used to determine the 1σ variations.

7.4.3 Field scale

Hall-probes located on the tracker provided measurements of the magnetic field strength within the tracking volume at known positions. An optimal field model was produced with a scale factor that optimally reproduced the Hall-probe measurements. Two additional field models were produced which used scale factors that were one standard deviation above and below the nominal value.

7.4.4 Field alignment

A field-alignment algorithm was developed based on the determination of the orientation of the field with respect to the mechanical axis of the tracker using coaxial tracks with $p_t \approx 0$ [39]. The optimal field model was created such that the simulated alignment is in agreement with the measurements. Two additional models that vary the alignment by one standard deviation were also produced.

7.4.5 Field uniformity

A Comsol [40] model of the field was used to generate the optimal model which includes the field generated by each coil using the 'as-built' parameters and the partial return yoke, which can cause variations in the on axis field by several percent. A simple field model was created using only the individual coil geometries to provide additional information on the effect of field uniformity on the reconstruction. The values for this field were normalised to the Hall-probe measurements as for the other field models. This represents a significant deviation from the COMSOL model, but demonstrates the stability of the reconstruction with respect to changes in field uniformity as the variation in emittance between all proposed field models is small

For each of the 5 field models, multiple 2000-muon ensembles were generated for each momentum bin. The deviation of the calculated emittance from the true emittance was found for each ensemble. The distribution of the difference between the ensemble emittance and the true emittance was assumed to be Gaussian with mean ε and variance $s^2 = \sigma^2 + \theta^2$, where σ is the theoretical statistical uncertainty and θ is an additional systematic error. The systematic bias for each momentum bin was then calculated as [41]:

$$b = \langle \varepsilon \rangle - \varepsilon_{\text{true}} \, ; \tag{4}$$

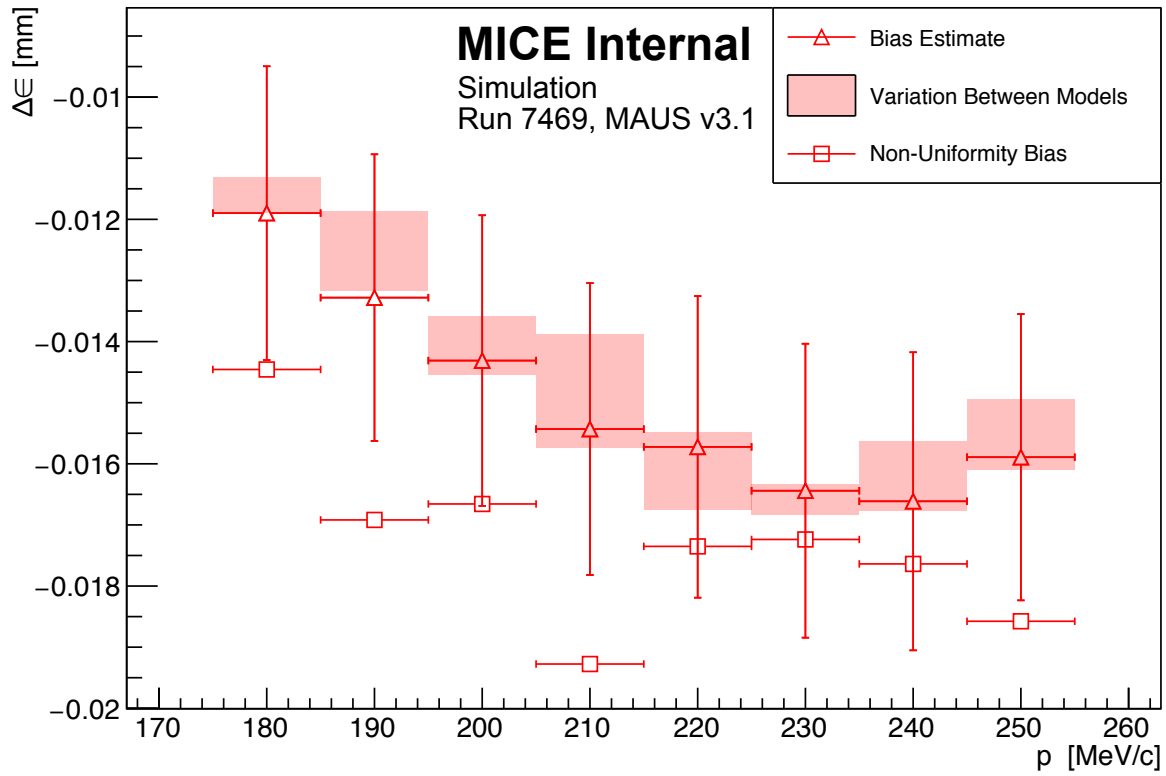

Figure 8: The systematic bias and uncertainty on the reconstructed emittance under different magnetic field model assumptions. The bias estimate (open triangles) includes the shown non-uniformity bias (open squares). The variation between the models (see text) is indicated by the shaded bands.

where $\varepsilon_{\text{true}}$ is the true beam emittance in that momentum bin and $\langle\varepsilon\rangle$ is the mean emittance from the N ensembles. The systematic uncertainty was calculated assuming that the distribution of residuals of ε_i from the mean $\langle\varepsilon\rangle$, satisfies a χ^2 distribution with $N-1$ degrees of freedom:

$$\chi^2_{N-1} = \sum_i^N \frac{(\varepsilon_i - \langle\varepsilon\rangle)^2}{\sigma^2 + \theta^2}\,; \tag{5}$$

and θ was estimated by minimising the expression $(\chi^2_{N-1} - (N-1))^2$ [41].

The uncertainty, θ, was consistent with zero in all momentum bins, whereas the bias, b, was found to be momentum dependent, as shown in figure 8. The bias was estimated from the mean difference between the reconstructed and true emittance values using the optimal field model. The variation in the bias was calculated from the range of values reconstructed for each of the additional field models. The model representing the effects of non-uniformities in the field was considered separately due to the significance of the deviation from the optimal model.

The results show a consistent systematic bias of ≈ -0.015 mm with momentum, p. The absolute variation in the mean values between the models that were used was smaller than the expected statistical fluctuations, demonstrating the stability of the reconstruction across the expected variations in field alignment and scale. The effect of the non-uniformity model was larger but still demonstrates consistent reconstruction in cases where non-physical fields are being used. The biases calculated from the optimal field model were used to the correct the emittance values in the final calculation (Section 7.5).

Table 3: Statistical and systematic uncertainties and biases, on the measured emittance as a function of mean momentum, $\langle p \rangle$.

Source	$\langle p \rangle$ (MeV/c)						
	190	200	210	220	230	240	250
Measured emittance (mm rad)	3.40	3.65	3.69	3.65	3.69	3.62	3.31
Statistical uncertainty	± 0.04	± 0.04	± 0.05	± 0.06	± 0.07	± 0.08	± 0.09
Beam selection:							
Diffuser aperture	$^{+0.05}_{-0.04}$	$^{+0.05}_{-0.05}$	$^{+0.05}_{-0.06}$	$^{+0.05}_{-0.05}$	$^{+0.04}_{-0.04}$	$^{+0.11}_{-0.05}$	$^{+0.04}_{-0.10}$
$\frac{\chi^2}{N_{\mathrm{DOF}}} \leq 4$	$^{+0.01}_{-0.00}$	$^{+0.00}_{-0.00}$	$^{+0.01}_{-0.00}$	$^{+0.00}_{-0.00}$	$^{+0.00}_{-0.00}$	$^{+0.01}_{-0.01}$	$^{+0.01}_{-0.00}$
Muon hypothesis	$^{+0.00}_{-0.00}$	$^{+0.00}_{-0.01}$	$^{+0.01}_{-0.00}$	$^{+0.00}_{-0.00}$	$^{+0.00}_{-0.01}$	$^{+0.01}_{-0.07}$	$^{+0.01}_{-0.00}$
Beam selection (Overall)	$^{+0.05}_{-0.04}$	$^{+0.05}_{-0.05}$	$^{+0.05}_{-0.06}$	$^{+0.05}_{-0.05}$	$^{+0.04}_{-0.04}$	$^{+0.11}_{-0.08}$	$^{+0.04}_{-0.10}$
Binning in p	± 0.02	± 0.02	± 0.02	± 0.03	± 0.03	± 0.04	± 0.05
Magnetic field misalignment and scale:							
Bias	-0.01	-0.01	-0.02	-0.02	-0.02	-0.02	-0.02
Uncertainty	0.00	0.00	0.00	0.00	0.00	0.00	0.00
Tracker resolution	± 0.00	± 0.00	± 0.00	± 0.00	± 0.01	± 0.01	± 0.01
Total systematic uncertainty	$^{+0.05}_{-0.04}$	± 0.06	± 0.06	± 0.06	± 0.05	$^{+0.12}_{-0.09}$	$^{+0.07}_{-0.11}$
Corrected emittance (mm rad)	3.41	3.66	3.71	3.67	3.71	3.65	3.34
Total uncertainty	± 0.06	± 0.07	$^{+0.07}_{-0.08}$	± 0.08	± 0.09	$^{+0.14}_{-0.13}$	$^{+0.12}_{-0.14}$
Total uncertainty (%)	$^{+1.90}_{-1.63}$	$^{+1.96}_{-1.94}$	$^{+2.01}_{-2.15}$	$^{+2.19}_{-2.34}$	$^{+2.40}_{-2.37}$	$^{+3.97}_{-3.49}$	$^{+3.47}_{-4.30}$

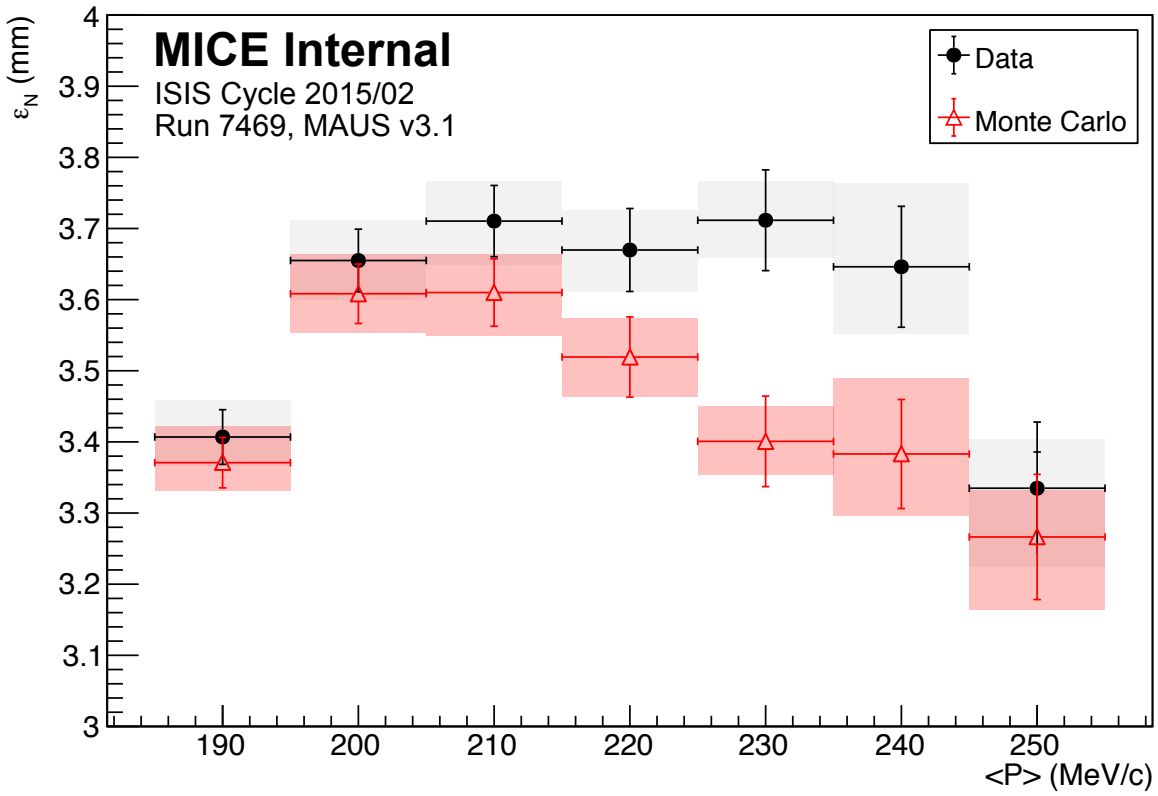

Figure 9: Normalised transverse emittance as a function of momentum, p, for data (black, filled circle) and reconstructed Monte Carlo (red, open triangle). The statistical uncertainty is shown by the error bars and the systematic uncertainty is shown by the shaded bands.

7.5 Emittance

The normalised transverse emittance as a function of p is shown in figure 9. The emittance has been corrected for the systematic bias shown in table 3. The uncertainties plotted are those summarised in table 3, where the bars represent the statistical uncertainty and the coloured bands the systematic uncertainty. The emittance is approximately flat between $195 \leq p \leq 245\,\text{MeV}/c$, corresponding to the region where the majority of the beam propagates along the design axis of the experiment. The mean emittance in this region is $\approx 3.7\,\text{mm}$. The emittance of the reconstructed Monte Carlo is consistently lower than that of the data.

Acknowledgements

The work described here was made possible by grants from Department of Energy and National Science Foundation (USA), the Instituto Nazionale di Fisica Nucleare (Italy), the Science and Technology Facilities Council (UK), the European Community under the European Commission Framework Programme 7 (AIDA project, grant agreement no. 262025, TIARA project, grant agreement no. 261905, and EuCARD), the Japan Society for the Promotion of Science and the Swiss National Science Foundation, in the framework of the SCOPES programme. We gratefully acknowledge all sources of support. We are grateful to the support given to us by the staff of the STFC Rutherford Appleton and Daresbury Laboratories. We acknowledge the use of Grid computing resources deployed and operated by GridPP in the UK, http://www.gridpp.ac.uk/.

References

[1] S. Geer, "Neutrino beams from muon storage rings: Characteristics and physics potential," *Phys. Rev.* **D57** (1998) 6989–6997, arXiv:hep-ph/9712290.

[2] M. Apollonio *et al.*, "Oscillation physics with a neutrino factory," hep-ph/0210192.

[3] D. V. Neuffer and R. B. Palmer, "A High-Energy High-Luminosity $\mu^+ - \mu^-$ Collider," *Conf. Proc.* **C940627** (1995) 52–54.

[4] R. B. Palmer, "Muon Colliders," *Rev. Accel. Sci. Tech.* **7** (2014) 137–159.

[5] M. Boscolo, M. Antonelli, O. R. Blanco-Garcia, S. Guiducci, S. Liuzzo, P. Raimondi, and F. Collamati, "Studies of a scheme for Low EMittance Muon Accelerator with production from positrons on target," arXiv:1803.06696 [physics.acc-ph].

[6] S. Y. Lee, *Accelerator Physics (Third Edition)*. World Scientific Publishing Co, 2012.

[7] S. Schröder, R. Klein, N. Boos, M. Gerhard, R. Grieser, G. Huber, A. Karafillidis, M. Krieg, N. Schmidt, T. Kühl, R. Neumann, V. Balykin, M. Grieser, D. Habs, E. Jaeschke, D. Krämer, M. Kristensen, M. Music, W. Petrich, D. Schwalm, P. Sigray, M. Steck, B. Wanner, and A. Wolf, "First laser cooling of relativistic ions in a storage ring," *Phys. Rev. Lett.* **64** (Jun, 1990) 2901–2904. http://link.aps.org/doi/10.1103/PhysRevLett.64.2901.

[8] J. S. Hangst, M. Kristensen, J. S. Nielsen, O. Poulsen, J. P. Schiffer, and P. Shi, "Laser cooling of a stored ion beam to 1 mk," *Phys. Rev. Lett.* **67** (Sep, 1991) 1238–1241. http://link.aps.org/doi/10.1103/PhysRevLett.67.1238.

[9] P. J. Channell, "Laser cooling of heavy ion beams," *Journal of Applied Physics* **52** no. 6, (1981) 3791–3793, http://dx.doi.org/10.1063/1.329218. http://dx.doi.org/10.1063/1.329218.

[10] J. Marriner, "Stochastic cooling overview," *Nucl. Instrum. Meth.* **A532** (2004) 11–18, arXiv:physics/0308044 [physics].

[11] V. V. Parkhomchuk and A. N. Skrinsky, "Electron cooling: 35 years of development," *Physics-Uspekhi* **43** no. 5, (2000) 433–452. http://stacks.iop.org/1063-7869/43/i=5/a=R01.

[12] A. N. Skrinsky and V. V. Parkhomchuk, "Cooling Methods for Beams of Charged Particles. (In Russian)," *Sov. J. Part. Nucl.* **12** (1981) 223–247. [Fiz. Elem. Chast. Atom. Yadra12,557(1981)].

[13] D. Neuffer, "Principles and Applications of Muon Cooling," *Conf.Proc.* **C830811** (1983) 481.

[14] D. Neuffer, "Principles and Applications of Muon Cooling," *Part. Accel.* **14** (1983) 75–90.

[15] The MICE collaboration, "INTERNATIONAL MUON IONIZATION COOLING EXPERIMENT." http://mice.iit.edu.

[16] **ISS Accelerator Working Group** Collaboration, M. Apollonio *et al.*, "Accelerator design concept for future neutrino facilities," *JINST* **4** (2009) P07001, arXiv:0802.4023 [physics.acc-ph].

[17] J. B. Rosenzweig, *Fundamentals of Beam Physics*. Oxford University Press, 2003.

[18] **Mice Collaboration** Collaboration, R. Bertoni *et al.*, "The design and commissioning of the MICE upstream time-of-flight system," *Nucl.Instrum.Meth.* **A615** (2010) 14–26, arXiv:1001.4426 [physics.ins-det].

[19] R. Bertoni, M. Bonesini, A. de Bari, G. Cecchet, Y. Karadzhov, and R. Mazza, "The construction of the MICE TOF2 detector." http://mice.iit.edu/micenotes/public/pdf/MICE0286/MICE0286.pdf, 2010.

[20] L. Cremaldi, D. A. Sanders, P. Sonnek, D. J. Summers, and J. Reidy, Jr, "A Cherenkov Radiation Detector with High Density Aerogels," *IEEE Trans. Nucl. Sci.* **56** (2009) 1475–1478, arXiv:0905.3411 [physics.ins-det].

[21] M. Ellis *et al.*, "The design, construction and performance of the MICE scintillating fibre trackers," *Nucl. Instrum. Meth.* **A659** (2011) 136–153, arXiv:1005.3491 [physics.ins-det].

[22] **MICE collaboration** Collaboration, M. Bogomilov *et al.*, "The MICE Muon Beam on ISIS and the beam-line instrumentation of the Muon Ionization Cooling Experiment," *JINST* **7** (2012) P05009, arXiv:1203.4089 [physics.acc-ph].

[23] F. Ambrosino *et al.*, "Calibration and performances of the KLOE calorimeter," *Nucl. Instrum. Meth.* **A598** (2009) 239–243.

[24] R. Asfandiyarov *et al.*, "The design and construction of the MICE Electron-Muon Ranger," *JINST* **11** no. 10, (2016) T10007, arXiv:1607.04955 [physics.ins-det].

[25] C. N. Booth *et al.*, "The design, construction and performance of the MICE target," *JINST* **8** (2013) P03006, arXiv:1211.6343 [physics.ins-det].

[26] C. N. Booth *et al.*, "The design and performance of an improved target for MICE," *JINST* **11** no. 05, (2016) P05006, arXiv:1603.07143 [physics.ins-det].

[27] **MICE** Collaboration, D. Adams *et al.*, "Characterisation of the muon beams for the Muon Ionisation Cooling Experiment," *Eur. Phys. J.* **C73** no. 10, (2013) 2582, arXiv:1306.1509 [physics.acc-ph].

[28] A. Dobbs, C. Hunt, K. Long, E. Santos, M. A. Uchida, P. Kyberd, C. Heidt, S. Blot, and E. Overton, "The reconstruction software for the MICE scintillating fibre trackers," *JINST* **11** no. 12, (2016) T12001, arXiv:1610.05161 [physics.ins-det].

[29] S. Blot, "Proton Contamination Studies in the MICE Muon Beam Line," *Proceedings 2nd International Particle Accelerator Conference (IPAC 11) 4-9 September 2011, San Sebastian, Spain* (2011) .

[30] T. Roberts *et al.*, "G4beamline; a "Swiss Army Knife" for Geant4, optimized for simulating beamlines." http://www.muonsinc.com/muons3/tiki-index.php?page=G4beamline.

[31] D. Rajaram and C. Rogers, "The mice offline computing capabilities." http://mice.iit.edu/micenotes/public/pdf/MICE0439/MICE0439.pdf , 2014. MICE Note 439.

[32] **GEANT4** Collaboration, S. Agostinelli *et al.*, "Geant4: A simulation toolkit," *Nuclear Instruments and Methods in Physics Research A* **506** (2003) 250–303.

[33] J. Allison *et al.*, "Geant4 developments and applications," *IEEE Trans. Nucl. Sci.* **53** (2006) 270–278.

[34] R. Brun and F. Rademakers, "ROOT: An object oriented data analysis framework," *Nucl. Instrum. Meth.* **A389** (1997) 81–86.

[35] **MICE** Collaboration, M. Bogomilov *et al.*, "Pion contamination in the MICE muon beam," *JINST* **11** no. 03, (2016) P03001, arXiv:1511.00556 [physics.ins-det].

[36] J. Cobb, "Statistical Errors on Emittance Measurements." http://mice.iit.edu/micenotes/public/pdf/MICE341/MICE268.pdf, 2009.

[37] J. Cobb, "Statistical Errors on Emittance and Optical Functions." http://mice.iit.edu/micenotes/public/pdf/MICE341/MICE341.pdf, 2011.

[38] J. H. Cobb, "Statistical errors on emittance." Unpublished., 2015.

[39] C. Hunt, "Mice note in preparation,".

[40] HTTP://WWW.COMSOL.COM/.

[41] L. Lyons, "On estimating systematic errors from repeated measurements," *Journal of Physics A: Mathematical and General* **25** no. 7, (1992) 1967. http://stacks.iop.org/0305-4470/25/i=7/a=035.

The MICE collaboration

M. Bogomilov, R. Tsenov, G. Vankova-Kirilova
Department of Atomic Physics, St. Kliment Ohridski University of Sofia, Sofia, Bulgaria

Y. Song, J. Tang
Institute of High Energy Physics, Chinese Academy of Sciences, Beijing, China

Z. Li
Sichuan University, China

R. Bertoni, M. Bonesini, F. Chignoli, R. Mazza
Sezione INFN Milano Bicocca, Dipartimento di Fisica G. Occhialini, Milano, Italy

V. Palladino
Sezione INFN Napoli and Dipartimento di Fisica, Università Federico II, Complesso Universitario di Monte S. Angelo, Napoli, Italy

A. de Bari, G. Cecchet
Sezione INFN Pavia and Dipartimento di Fisica, Pavia, Italy

D. Orestano, L. Tortora
INFN Sezione di Roma Tre and Dipartimento di Matematica e Fisica, Università Roma Tre, Italy

Y. Kuno
Osaka University, Graduate School of Science, Department of Physics, Toyonaka, Osaka, Japan

S. Ishimoto
High Energy Accelerator Research Organization (KEK), Institute of Particle and Nuclear Studies, Tsukuba, Ibaraki, Japan

F. Filthaut[1]
Nikhef, Amsterdam, The Netherlands

D. Jokovic, D. Maletic, M. Savic
Institute of Physics, University of Belgrade, Serbia

O. M. Hansen, S. Ramberger, M. Vretenar
CERN, Geneva, Switzerland

R. Asfandiyarov, A. Blondel, F. Drielsma, Y. Karadzhov
DPNC, Section de Physique, Université de Genève, Geneva, Switzerland

G. Charnley, N. Collomb, A. Gallagher, A. Grant, S. Griffiths, T. Hartnett, B. Martlew, A. Moss, A. Muir, I. Mullacrane, A. Oates, P. Owens, G. Stokes, M. Tucker, P. Warburton, C. White

[1] Also at Radboud University, Nijmegen, The Netherlands

STFC Daresbury Laboratory, Daresbury, Cheshire, UK

D. Adams, R.J. Anderson, P. Barclay, V. Bayliss, J. Boehm, T. W. Bradshaw, M. Courthold, K. Dumbell, V. Francis, L. Fry, T. Hayler, M. Hills, A. Lintern, C. Macwaters, A. Nichols, R. Preece, S. Ricciardi, C. Rogers, T. Stanley, J. Tarrant, A. Wilson
STFC Rutherford Appleton Laboratory, Harwell Oxford, Didcot, UK

S. Watson
STFC Rutherford UK Astronomy Technology Centre, Royal Observatory, Edinburgh, Blackford Hill, Edinburgh EH9 3HJ, UK

R. Bayes, J. C. Nugent, F. J. P. Soler
School of Physics and Astronomy, Kelvin Building, The University of Glasgow, Glasgow, UK

R. Gamet
Department of Physics, University of Liverpool, Liverpool, UK

G. Barber, V. J. Blackmore, D. Colling, A. Dobbs, P. Dornan, C. Hunt, A. Kurup, J-B. Lagrange, K. Long, J. Martyniak, S. Middleton, J. Pasternak, M. A. Uchida
Department of Physics, Blackett Laboratory, Imperial College London, London, UK

J. H. Cobb, W. Lau
Department of Physics, University of Oxford, Denys Wilkinson Building, Oxford, UK

C. N. Booth, P. Hodgson, J. Langlands, E. Overton, M. Robinson, P. J. Smith, S. Wilbur
Department of Physics and Astronomy, University of Sheffield, Sheffield, UK

A. J. Dick, K. Ronald, C. G. Whyte, A. R. Young
SUPA and the Department of Physics, University of Strathclyde, Glasgow, UK

S. Boyd, P. Franchini, J. R. Greis, C. Pidcott, I. Taylor
Department of Physics, University of Warwick, Coventry, UK

R.B.S. Gardener, P. Kyberd, J. J. Nebrensky
Brunel University, Uxbridge, UK

M. Palmer, H. Witte
Brookhaven National Laboratory, NY, USA

A. D. Bross, D. Bowring, A. Liu, D. Neuffer, M. Popovic, P. Rubinov
Fermilab, Batavia, IL, USA

A. DeMello, S. Gourlay, D. Li, S. Prestemon, S. Virostek, M. Zisman[1]
Lawrence Berkeley National Laboratory, Berkeley, CA, USA

B. Freemire, P. Hanlet, D. M. Kaplan, T. A. Mohayai, D. Rajaram, P. Snopok, V. Suezaki, Y. Torun
Illinois Institute of Technology, Chicago, IL, USA

Y. Onel
Department of Physics and Astronomy, University of Iowa, Iowa City, IA, USA

L. M. Cremaldi, D. A. Sanders, D. J. Summers
University of Mississippi, Oxford, MS, USA

G. G. Hanson, C. Heidt
University of California, Riverside, CA, USA